Digital Restoration of Indium-111 and Iodine-123 SPECT Images with Optimized Metz Filters

Michael A. King, Ronald B. Schwinger, Bill C. Penney, Paul W. Doherty, and Jesus A. Bianco

Department of Nuclear Medicine, The University of Massachusetts Medical Center, Worcester, Massachusetts

A number of radiopharmaceuticals of great current clinical interest for imaging are labeled with radionuclides that emit medium- to high-energy photons either as their primary radiation, or in low abundance in addition to their primary radiation. The imaging characteristics of these radionuclides result in gamma camera image quality that is inferior to that of ^{99m}Tc images. Thus, in this investigation ^{111}In and ^{123}I contaminated with ~4% ^{124}I were chosen to test the hypothesis that a dramatic improvement in planar and SPECT images may be obtainable with digital image restoration. The count-dependent Metz filter is shown to be able to deconvolve the rapid drop at low spatial frequencies in the imaging system modulation transfer function (MTF) resulting from the acceptance of septal penetration and scatter in the camera window. Use of the Metz filter was found to result in improved spatial resolution as measured by both the full width at half maximum and full width at tenth maximum for both planar and SPECT studies. Two-dimensional, prereconstruction filtering with optimized Metz filters was also determined to improve image contrast, while decreasing the noise level for SPECT studies. A dramatic improvement in image quality was observed with the clinical application of this filter to SPECT imaging.

J Nucl Med 27:1327–1336, 1986

Many exciting radiopharmaceuticals are currently being labeled with radionuclides that emit medium- to high-energy photons either as their primary radiation or in low abundance in addition to their primary radiation (*1–7*). Images of the distribution of these radionuclides are of inferior quality compared with those obtained with technetium-99m (^{99m}Tc). These images typically have decreased image contrast because of septal penetration and scatter, poorer spatial resolution because of the collimators employed, and higher noise levels because of the lower activities administered. It was hypothesized that since digital image restoration techniques were able to significantly improve the quality of single photon emission computed tomographic (SPECT) images of the distribution of ^{99m}Tc-labeled agents (*8–11*), a dramatic improvement in image quality should be obtainable with digital restoration of images of radionuclides other than ^{99m}Tc. The present study is a preliminary investigation of this hypothesis. Images of agents labeled with indium-111 (^{111}In) or iodine-123 (^{123}I) contaminated with ~4% iodine-124 (^{124}I) (*12*) were selected to serve as examples for the improvements in image quality that could be obtained with medium- to high-energy photon emitters.

Received Aug. 23, 1985; revision accepted Jan. 15, 1986.

For reprints contact: Michael A. King, PhD, Dept. of Nuclear Medicine, The University of Massachusetts Medical Center, 55 Lake Ave. North, Worcester, MA 01605-2397.

MATERIALS AND METHODS

Determination of Modulation Transfer Functions

In digital image restoration, an estimate of the modulation transfer function (MTF) is used to characterize and partially correct for the blurring that occurs during acquisition. The MTFs employed with this study were determined from line spread functions (LSFs) (*13,14*) acquired with a large field-of-view, single headed, SPECT camera.* A 40-cm-long line source of 1.14-mm inner diam polyethylene tubing filled with ~75 MBq of the selected radionuclide was imaged to obtain the LSFs. For measurement of the LSFs in a scattering medium, the line source was positioned 7.5 cm deep in a 20-cm-thick stack of 40 × 40 × 2.54-cm sheets of Plexiglas. This depth was selected to be approximately that of the "effective" mean free path of ^{99m}Tc photons

and was also used for ^{111}In and ^{123}I to facilitate comparison between radionuclides. Plexiglas was selected as the scattering material since its mass attenuation coefficient is approximately equal to that of tissue over the photon energy range of interest herein, and it is easier to handle and position a line source in Plexiglas than in a large volume of water (*13*). The air gap between the face of the collimator and the surface of the scattering material was chosen to be 7.5 cm. This represents, in our clinical studies, the average distance between the collimator and patient during a standard, circular orbit SPECT acquisition. The collimators employed were either a low-energy, high resolution collimator (LEHR)† for ^{99m}Tc, or a medium-energy, medium sensitivity (MEMS)‡ collimator for ^{99m}Tc, ^{111}In, and ^{123}I. Technetium-99m was imaged by the MEMS collimator to determine the degradation in the MTF caused by solely switching to this collimator. Images of 10 million counts were acquired on a computer system in 128 × 128 pixel, word mode format with a pixel size of 3 mm. Care was taken to align the source along the Y-axis in the center of the field-of-view. Calculation of the MTF proceeded as follows. The average background count level per pixel was first subtracted from the images, and then the squared magnitudes of the Fourier transforms of eight individual rows (LSFs) near the center of the field-of-view were calculated. Each of these was the sum of the power spectrum of the line source and power spectrum of the Poisson noise. Since it has previously been shown that the average value of the noise power spectrum is the total count (*15*), the total count in each LSF was subtracted from the squared Fourier transform of each row. The results were then averaged and normalized to the zero frequency term, and the square root of each term calculated to yield the MTF.

The LSF for ^{123}I did not fall-off to zero at the edge of the field-of-view. Use of this truncated LSF directly, when calculating the MTF, resulted in a "ripple" artifact in the MTF (*16,17*). Thus, the LSF was multiplied by a Kaiser window with a form factor (beta) equal to 3.38 (*18*). This procedure smoothed the "ripple" artifact while broadening the MTF only slightly.

Count-Dependent Metz Filter

The restoration filter investigated for use with ^{111}In and ^{123}I images was the count-dependent Metz filter (*9,11,19*). The one-dimensional frequency domain form of the Metz filter is defined as (*20,21*):

$$M(f) = MTF(f)^{-1} \cdot [1 - (1 - MTF(f)^2)^X], \quad (1)$$

where MTF is the modulation transfer function, f is the spatial frequency, and X is a factor which controls the extent to which the inverse filter is followed before the Metz filter switches to noise suppression. This filter was made count-dependent by varying the parameter X of Eq. (1) as a function of the total image count (*19*). The mathematical criterion used for optimizing this relationship was the minimization of the normalized mean-squared error (NMSE) between the restored images, and the original nondegraded images (termed the "object" images) that would have been acquired if blurring and Poisson noise were not present. The object image from which simulated acquisition images were generated was that of a very high count acquisition of the Alderson liver and spleen organ phantoms filled with ^{99m}Tc (*11*). Five simulated images at each of five different count levels were used in the optimization of the filter for each MTF. The details of the optimization procedure can be found elsewhere (*11,19*).

It has been previously shown (*11,19*) that a lower NMSE and visually more pleasing images (less of a problem with textured noise) were obtained when a generalized exponential of the form

$$H(f) = \exp(-f^P/S) \quad (2)$$

was used instead of the "true" MTF in either solely the second term of Eq. (1) (low-pass filter term), or both the first and second terms. Here P is the exponent of the spatial frequency and S is a constant analogous to the variance of a Gaussian function. Use of the generalized exponential in just the second term of Eq. (1) provides a filter in which the deconvolution term and the low-pass filter term use different functions for the MTF and hence are independent. This form of the filter is used exclusively herein to prereconstruction filter the planar acquisition images.

Comparison of Image Quality

As measures of spatial resolution, the full width at half maximum (FWHM) and full width at tenth maximum (FWTM) of the LSF for planar images and the point spread function (PSF) for transverse SPECT slices were used. A 64-frame SPECT acquisition using a MEMS collimator was made of 15 cm long ^{111}In or ^{123}I line sources in the center of an elliptical Plexiglas cylinder. The face of this cylinder measured 22 cm by 30 cm and a hole for the line source tubing traversed its 15 cm depth. A circular rotation of the head about the phantom was employed with an average air gap of ~7.5 cm. For the planar images, the FWHM and FWTM were determined at five levels in the first projection image of the SPECT acquisition. For SPECT, these were measured in five slices of the line source reconstructed after filtering with a ramp filter (*22*), a ramp filter modified by a Shepp-Logan filter with a cutoff frequency of 0.66 times the Nyquist frequency (*22*), or with two-dimensional Metz filtering of the acquisition images followed by reconstruction with the ramp filter. The two-dimensional Metz filtering of the entire 64-frame SPECT acquisition required only 18 sec when using an array processor (*19*).§ The SPECT images were

reconstructed using standard software[*] adapted to run on the array processor. Attenuation correction was done using the arithmetic-mean method (*22*).

To study the effects of restoration filtering upon SPECT image contrast and noise level, five SPECT acquisitions of a standard SPECT phantom[**] (64 frames of 64 × 64 pixels each) at 150,000 counts/frame each for ^{111}In and ^{123}I were used. Studies of these parameters with ^{99m}Tc imaging have been previously reported (*11,19*). A 1 million count/frame acquisition for each radionuclide was also acquired. The acquisitions were performed using a MEMS collimator, 15% symmetric energy window(s) and an 18.5 cm radius of rotation so that an air gap of 7.5 cm from the phantom was maintained. The images were acquired with 1.5 magnification yielding a pixel size of 4 mm, and were uniformity corrected using a 50 million count cobalt-57 (^{57}Co) flood image. The ^{57}Co source was positioned 4 ft in front of the camera collimator to minimize the effects of nonuniformity in the source. The images were reconstructed as with the line sources. Regions of interest (ROIs) for the spheres were determined from the reconstruction of the single high-count acquisition performed for each radionuclide. For a 2-pixel-wide slice through the spheres, the magnitude of the image contrast was calculated for spheres of 1.59, 1.91, 2.54, and 3.18 cm in diam. The contrast was defined as (*11,19*):

$$C_i = [CP_S - CP_B]/CP_B, \quad (3)$$

where CP_S is the average count/pixel for the ROI selected for each sphere and CP_B is the average count/pixel in a background ROI. To assess the effects of filtering on noise levels, the percent fractional standard deviation (% FSD) for a 4 pixel wide annular ROI of the same radius as the distribution of the spheres in a slice through the phantom containing uniform activity was calculated.

The statistical significance of the variation in the FWHMs, FWTMs, image contrasts, and % FSDs between filters was determined using a one-way analysis of variance (*23,24*). When a significant difference was observed between the means of the various filters at a p value of ≤0.05, Sheffe's method of comparing paired means for a significant difference was used to compare each filtered result to the raw data values in the case of planar images, or to the ramp filter values in the case of SPECT images (*23,24*).

RESULTS

Figure 1 shows a comparison of five MTFs obtained with a large field-of-view SPECT camera. In all cases, the line source was a total of 15 cm from the face of the collimator. With the exception of MTF A, that was imaged with the source solely in air, the MTFs are for

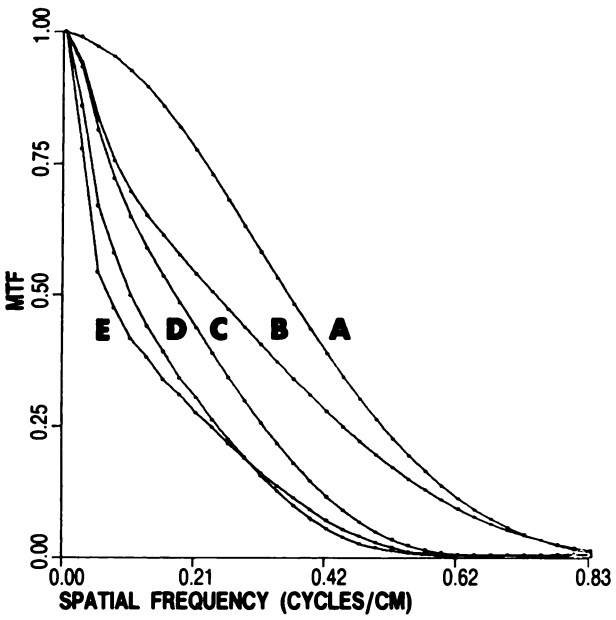

FIGURE 1
Plots of system modulation transfer functions (MTFs) for line source 15.0 cm from face of collimator and, with exception of A, positioned 7.5 cm deep in 20.0 cm of Plexiglas. From right to left MTFs are A: ^{99m}Tc imaged in air with low-energy, high resolution (LEHR) colimator; B: ^{99m}Tc imaged with LEHR collimator; C: ^{99m}Tc imaged with medium-energy, medium sensitivity collimator (MEMS); D: ^{111}In imaged with MEMS collimator; and E: ^{123}I imaged with MEMS collimator

line sources 7.5 cm deep in 20 cm of Plexiglas. In comparing these MTFs one can gain an appreciation for the magnitude, and spatial frequency range of importance, of the various causes of degradation of the MTF. MTFs A and B demonstrate the rapid fall at low spatial frequencies characteristic of scatter (*11,17,25,26*). From Figs. 1B and 1C, it can be seen that switching from a LEHR to a MEMS collimator, while still imaging ^{99m}Tc, causes a significant difference in the MTFs after the low spatial frequencies, but the low-frequency scatter degradation is about the same. Notice, however, that both ^{111}In and ^{123}I have a much more rapid drop at very low spatial frequencies than was noted for ^{99m}Tc. This is due, in large part, to the added septal penetration of medium- to high-energy photons being emitted by these radionuclides (*25,27–30*). In the case of septal penetration by photons of energy higher than that of the primary photons, they are included in the camera energy window through the process of Compton scattering in the crystal (*27*).

The effects of the degradation of the system MTF when imaging ^{123}I or ^{111}In on restoration filters is demonstrated in the comparison of count-dependent Metz filters for ^{99m}Tc and a LEHR collimator, ^{111}In and a MEMS collimator, and ^{123}I and a MEMS collimator given in Fig. 2. In this figure, spatial frequency is given

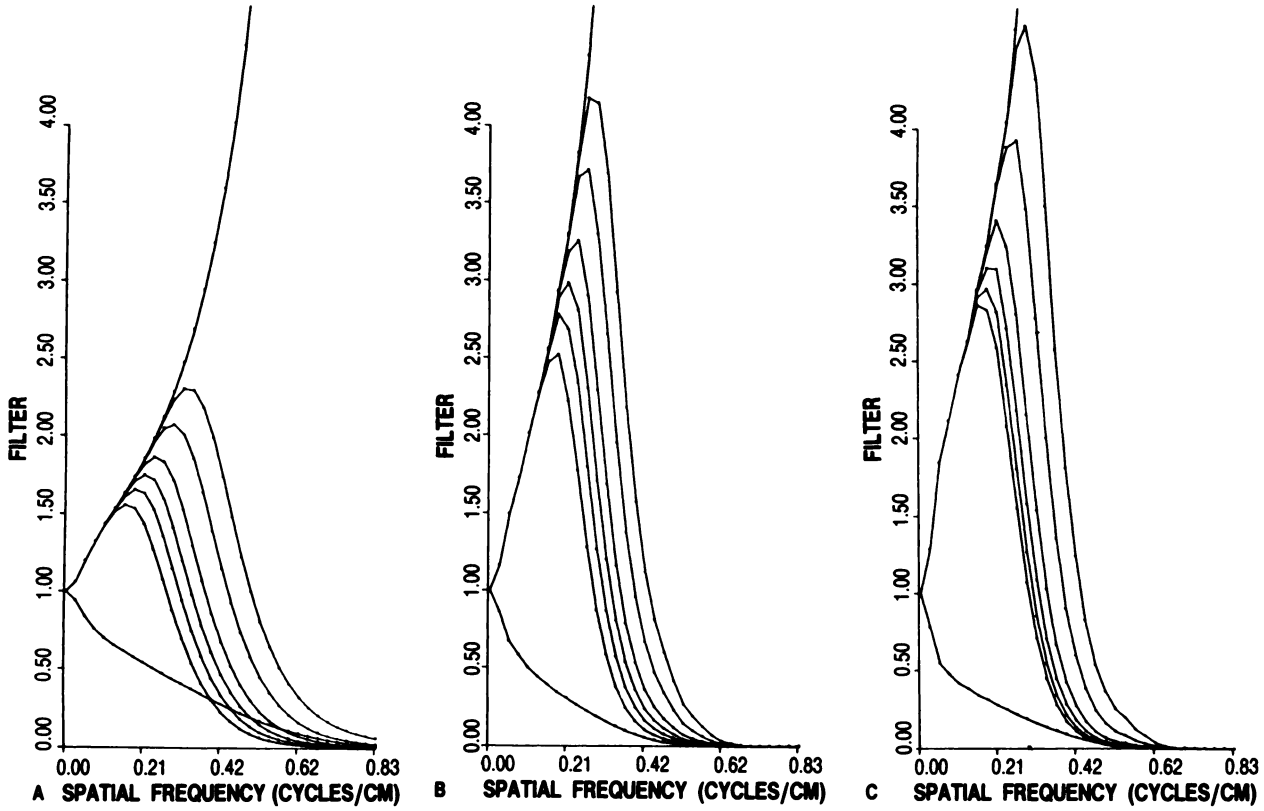

FIGURE 2
Plots of system MTF (lowest curve), inverse filter (highest curve), and six Metz filters for total counts of 20,000, 50,000, 100,000, 200,000, 500,000, or 1,000,000 (six curves in between) for A: Imaging ^{99m}Tc with LEHR collimator; B: Imaging ^{111}In with MEMS collimator; and C: Imaging ^{123}I with MEMS collimator. MTF and inverse filter (MTF^{-1}) are included in plot to show possible range of Metz filters as parameter X of Eq. (1) increases from 1.0 to infinity

in terms of cycles/cm. The maximum frequency shown is 0.25 cycles/pixel for a 128 × 128 pixel acquisition on our system (3-mm sampling bin width), and 0.5 cycles/pixel (Nyquist frequency) for a 64 × 64 pixel acquisition. The MTF (bottom curve) and inverse filter (MTF^{-1}) are included in each plot to show the possible range of Metz filters produced as X of Eq. (1) increases from 1.0 to infinity. Notice how far above 1.0 the ^{111}In and ^{123}I filters rise, even for low counts, in comparison with those optimized for ^{99m}Tc. This shows the increased deconvolution which occurs for ^{111}In and ^{123}I as opposed to ^{99m}Tc.

The filter parameters for these Metz filters are given in Table 1. X refers to the factor which controls noise suppression of Eq. (1), and P and S are the parameters of the generalized exponential of Eq. (2). In the case of the filters reported here, P is a constant for each radionuclide. X and S vary with the total number of counts in the image according to regression equations obtained by fitting simple functional forms to the values which yielded the minimum NMSE for the 25 simulated images for each MTF. The m's and b's listed in Table 1 are the slopes and intercepts obtained for the functional relation which yielded the largest regression correlation coefficient. Generally, this was a square root dependent relation of the form:

$$X \text{ (or S)} = m \cdot (\text{count})^{1/2} + b. \quad (4)$$

A direct variation with the total count of the form

$$X = m \cdot \text{count} + b \quad (5)$$

was observed to yield the largest value of the correlation coefficient of the functional relationships tested for X when imaging ^{123}I.

Tables 2 and 3 give an assessment of the effect of the

TABLE 1
Parameters Obtained for Optimized Metz Filter for Different Radionuclides and Collimators*

	X		P	S	
Radionuclide	m†	b		m	b
^{99m}Tc (LEHR)	0.052	4.1	1.30	0.0027	13.8
^{111}In (MEMS)	0.154	5.3	1.40	0.0011	11.3
^{123}I (MEMS)	0.000095‡	8.7‡	1.55	0.0021	18.8

* Imaging conditions were for 0.3 cm pixel size, line source 7.5 cm deep in 20 cm Plexiglas, and 7.5 cm air gap.

† m and b = Slope and intercept obtained for regression relations for X and S, respectively.

‡ Follows regression Eq. (5), rest follow regression Eq. (4).

TABLE 2
FWHM and FWTM for ^{111}In After Application of Various Filters

Item	FWHM (cm)	s.d. (cm)	FWTM (cm)	s.d. (cm)
Planar				
Raw Data	2.81	0.12	7.3	0.7
Shepp-Logan (0.66)*	3.23‡	0.10	7.9	0.5
Metz-^{99m}Tc (20k)†	2.46‡	0.05	4.3‡	0.2
Metz-^{99m}Tc (150k)†	2.26‡	0.05	4.0‡	0.1
Metz-^{99m}Tc (500k)†	2.09‡	0.05	3.7‡	0.1
Metz-^{111}In (20k)†	2.39‡	0.05	4.07‡	0.11
Metz-^{111}In (150k)†	2.09‡	0.04	3.56‡	0.07
Metz-^{111}In (500k)†	1.92‡	0.04	3.27‡	0.08
SPECT				
Ramp	2.26	0.08	4.04	0.08
Shepp-Logan (.66)*	2.40‡	0.06	4.28‡	0.07
Metz-^{99m}Tc (20k)†	2.38‡	0.02	4.13	0.03
Metz-^{99m}Tc (150k)†	2.22‡	0.03	3.84‡	0.04
Metz-^{99m}Tc (500k)†	2.09‡	0.03	3.59‡	0.05
Metz-^{111}In (20k)†	2.40‡	0.01	4.02	0.02
Metz-^{111}In (150k)†	2.11‡	0.01	3.52‡	0.04
Metz-^{111}In (500k)†	1.96‡	0.02	3.30‡	0.02

*Cutoff frequency for Shepp-Logan as multiple of Nyquist frequency for 0.4 cm pixel size.
†Count level input to count-dependent Metz filter.
‡Significant difference ($p < 0.05$) from ramp filter or raw data value.

TABLE 3
FWHM and FWTM for ^{123}I After Application of Various Filters

	FWHM (cm)	s.d. (cm)	FWTM (cm)	s.d. (cm)
Planar				
Raw Data	3.42	0.10	9.8	0.7
Shepp-Logan (0.66)*	3.52	0.08	8.9	0.8
Metz-^{99m}Tc (20k)†	2.89‡	0.04	5.10‡	0.09
Metz-^{99m}Tc (150k)†	2.68‡	0.05	4.69‡	0.10
Metz-^{99m}Tc (500k)†	2.62‡	0.07	4.59‡	0.12
Metz-^{123}I (20k)†	2.61‡	0.03	4.46‡	0.07
Metz-^{123}I (150k)†	2.50‡	0.03	4.26‡	0.07
Metz-^{123}I (500k)†	2.31‡	0.04	3.94‡	0.07
SPECT				
Ramp	2.74	0.08	4.87	0.17
Shepp-Logan (0.66)*	2.86‡	0.07	5.10‡	0.14
Metz-^{99m}Tc (20k)†	2.77	0.03	4.82	0.05
Metz-^{99m}Tc (150k)†	2.54‡	0.03	4.40‡	0.07
Metz-^{99m}Tc (500k)†	2.45‡	0.04	4.26‡	0.08
Metz-^{123}I (20k)†	2.65	0.02	4.45‡	0.04
Metz-^{123}I (150k)†	2.53‡	0.03	4.25‡	0.05
Metz-^{123}I (500k)†	2.32‡	0.03	3.94‡	0.06

*Cutoff frequency for Shepp-Logan as multiple of Nyquist frequency for 0.4 cm pixel size.
†Count level input to count-dependent Metz filter.
‡Significant difference ($p < 0.05$) from ramp filter or raw data value.

Metz filter upon spatial resolution for ^{111}In and ^{123}I sources, respectively, for both planar and SPECT images. The Metz filters in these tables are compared against a Shepp-Logan filter with cutoff frequency of 0.66 times the Nyquist frequency (*22*) that was selected as an example of a low-pass filter. Notice that for both planar and SPECT images, as the total count input to the Metz filter increases, the FWHM and FWTM decreases and thus spatial resolution improves as one would predict from Fig. 2. The three count levels for which the count-dependent Metz filters were tested were chosen to span the range of counts observed in SPECT studies (20–150k), and to be equal to that of an average static acquisition (500k). The tables show that a decrease in FWHM and FWTM is observed when the Metz filter optimized for the actual radionuclide and collimator employed in imaging is used to digitally filter the images. Notice also that the Metz filter is more effective at decreasing the FWTM than the FWHM. This difference was even more apparent when viewing the LSFs. The Metz filtered LSFs, even for low counts, had the long tails of the LSFs which are due to scatter and septal penetration, markedly diminished or removed.

A further appreciation for the improvement in SPECT image quality with the use of the Metz filter for restoring ^{111}In and ^{123}I images can be obtained from Tables 4 and 5. These tables list the average image contrast for the Plexiglas spheres and the % FSD for an area of uniform activity obtained from images of a SPECT phantom pre-reconstruction filtered by various techniques. When comparing the contrasts reported in these tables, it should be remembered that the true object contrast is 1.0. Notice that for both radionuclides

TABLE 4
Image Contrast and Fractional Standard Deviation for Five 150,000 Counts/Frame Acquisitions of SPECT Phantom Filled with ^{111}In

Filter	Image contrast* (cm) 3.18	2.54	1.91	1.59	% FSD†
RAMP	0.26	0.12	0.04	0.03	21.4
	(0.03)	(0.08)	(0.06)	(0.08)	(1.4)
Shepp-Logan (0.66)‡	0.22	0.09	0.02	0.01	14.0**
	(0.03)	(0.05)	(0.02)	(0.05)	(1.9)
Metz-^{99m}Tc§	0.48**	0.26	0.17	0.08	11.0**
	(0.03)	(0.07)	(0.07)	(0.10)	(1.2)
Metz-^{111}In¶	0.63**	0.34**	0.24**	0.13	12.3**
	(0.02)	(0.10)	(0.11)	(0.11)	(0.7)

*Average (s.d.) image contrast for five different acquisitions at this count level for given size Plexiglas sphere.
†Average (s.d.) percent fractional standard deviation for counts in annular region of interest in slice above spheres located in region of uniform activity.
‡Cutoff frequency of Shepp-Logan filter as multiple of Nyquist frequency for 0.4 cm pixel size.
§Metz optimized for ^{99m}Tc and LEHR collimator.
¶Metz optimized for ^{111}In and MEMS collimator.
**Significantly different ($p < 0.05$) from ramp filter.

TABLE 5
Image Contrast and Fractional Standard Deviation for Five 150,000 Counts/Frame Acquisitions of SPECT Phantom Filled with ^{123}I

Filter	Image contrast* (cm) 3.18	2.54	1.91	1.59	% FSD†
RAMP	0.32	0.29	0.20	0.08	22.1
	(0.04)	(0.04)	(0.08)	(0.11)	(0.8)
Shepp-Logan (0.66)‡	0.29	0.25	0.16	0.05	10.9**
	(0.04)	(0.04)	(0.07)	(0.09)	(0.4)
Metz-^{99m}Tc§	0.46**	0.37**	0.23	0.12	7.6**
	(0.06)	(0.02)	(0.05)	(0.07)	(0.6)
Metz-^{123}I¶	0.66**	0.50**	0.31	0.15	7.8**
	(0.06)	(0.03)	(0.05)	(0.08)	(0.4)

* Average (s.d.) image contrast for five different acquisitions at this count level for given size Plexiglas sphere.

† Average (s.d.) percent fractional standard deviation for counts in an annular region of interest in slice above the spheres located in a region of uniform activity.

‡ Cutoff frequency of Shepp-Logan filter as multiple of Nyquist frequency for 0.4 cm pixel size.

§ Metz optimized for ^{99m}Tc and LEHR collimator.

¶ Metz optimized for ^{123}I and MEMS collimator.

** Significantly different ($p < 0.05$) from ramp filter.

a significant increase in image contrast of the spheres coupled with a decrease in noise level is observed with use of Metz filtering.

A visual comparison of the difference in image quality that use of the Metz filter provides with ^{123}I imaging can be appreciated in Fig. 3 which shows reconstructed slices through the SPECT phantom filled with ^{123}I at the level of the spheres. Notice that use of the Metz filter increases the contrast of the spheres while decreasing the noise level. Also notice that the spheres appear larger than their actual size with Metz prefiltering, especially in the case of image D. This is because the spatial resolution of the imaging system even after filtering (Table 3) is such that each sphere is blurred into a larger area of less than its true contrast (Table 5). The reason why the spheres of image D appear larger than in image C is that use of the Metz filter optimized for ^{123}I rather than ^{99m}Tc cleaned up scatter and septal penetration better. This can be seen by noting that the FWHMs are about the same for the two filters (Table 3), but the tails of ^{123}I LSFs were diminished to a much greater extent with the use of the Metz filter optimized for ^{123}I as evidenced by the greater contrasts (Table 5) and smaller FWTMs (Table 3). Thus the true degree of blurring at the FWHM level is better appreciated in the ^{123}I Metz filtered image of Fig. 3D. One should also note the appearance of the noise "blobs" in Fig. 3. These also appear more spread out in image D. The presence and appearance of noise artifacts should always be kept in mind whenever digital filtering is used.

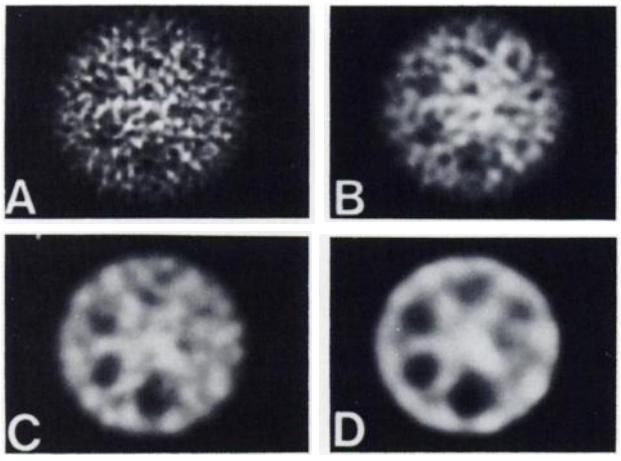

FIGURE 3
Reconstructed transverse slice from acquisition of SPECT phantom filled with ^{123}I acquired for 150,000 counts per frame. Phantom has six Plexiglas spheres of 0.95, 1.27, 1.59, 1.91, 2.54, and 3.18 cm diam spaced 60° apart. A: Ramp filter. B: Shepp-Logan filter with cutoff frequency of 0.66 times the Nyquist frequency. C: Filtered by Metz filter optimized for ^{99m}Tc and LEHR collimator. D: Filtered by Metz filter optimized for ^{123}I and MEMS collimator

The Metz filters have been applied to our clinical SPECT studies of ^{111}In- and ^{123}I-labeled imaging agents with dramatic results. Figure 4 illustrates the difference in image quality obtained when the Metz filter optimized for ^{111}In is used to prereconstruction filter an ^{111}In-labeled monoclonal antibody SPECT study (*2*). It can be seen that the use of the Metz filter allows the right kidney to be distinguished from the liver in the first slice on the left. It is also clear that the lesions in the liver are best seen in the ^{111}In optimized Metz filtered reconstruction. These lesions were confirmed by a ^{99m}Tc liver/spleen study, and by ultrasound. Approximately 64,000 counts per acquisition frame were collected for this study. Thus this image was processed by Metz filters similar to those for 50,000 counts in Figs. 2A and 2B.

Figure 5 shows that use of the Metz filter optimized for ^{123}I can transform nearly featureless ^{123}I-labeled iodamphetamine brain SPECT images (*3,4*) into images that provide clear anatomic structures. It has also been shown that a significant improvement in image quality of ^{123}I brain flow SPECT images is possible with prereconstruction, two-dimensional filtering using a bandpass enhancement filter (*31*). There were ~48,000 counts per acquisition frame in this study. Thus Metz filters similar to those for 50,000 counts in Figs. 2A and 2C were used in filtering it prereconstruction.

DISCUSSION

The inferior quality of images of radionuclides that emit medium- to high-energy photons compared with those of ^{99m}Tc lead to the hypothesis that a truly significant increase in SPECT image quality could be ob-

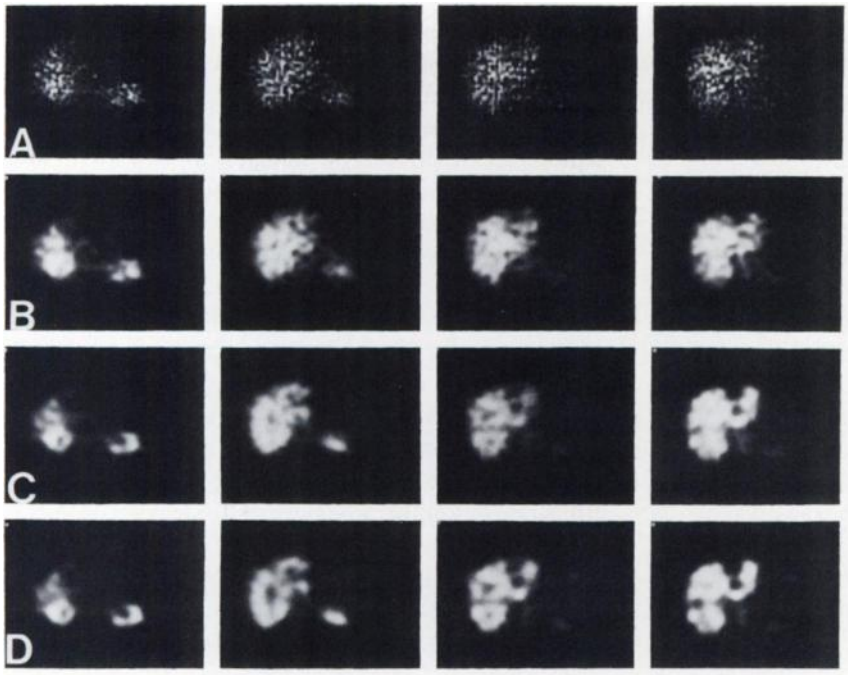

FIGURE 4
Selected reconstructed transverse slices of the liver from SPECT acquisition of ^{111}In-labeled monoclonal antibody study. Row A: Ramp filter. Row B: Shepp-Logan filter with cutoff frequency 0.66 times Nyquist frequency. Row C: Filtered by Metz filter optimized for ^{99m}Tc and LEHR collimator. Row D: Filtered by Metz filter optimized for ^{111}In and MEMS collimator. First column on left is through kidneys and inferior portion of right lobe of liver. Differentiation between renal and hepatic tissue is best made with Metz filter optimized for ^{111}In. In next three columns, defects corresponding to focal metastases that did not accumulate antibody are present in both right and left lobes. Note that their presence is best appreciated in row D, the row restored with filter for ^{111}In. Their presence was confirmed by other imaging modalities

tained with digital restoration techniques optimized for such radionuclides. The results obtained here show that significant improvements in spatial resolution (Tables 2 and 3), image contrast (Tables 4 and 5), and noise level (Tables 4 and 5) can be readily obtained with use of the Metz filter optimized for use with ^{111}In and ^{123}I. The dramatic improvements in the appearance of the clinical SPECT images with application of restoration filters (Figs. 4 and 5) verify the predictions for improved image quality made based upon the above objective measurements. These results suggest that similar improvements in image quality should be obtainable for other radionuclides that emit medium to high energy photons. For instance, one would expect to find improvements with gallium-67 (^{67}Ga) citrate SPECT imaging of lymphoma and lung carcinoma (*3*). A marked increase in the quality of images of the distribution of ^{131}I-labeled antibodies (*1*) and new ^{131}I-labeled adrenal tumor imaging agents (*6*) should also occur. The imaging of positron emitters such as rubidium-82 for

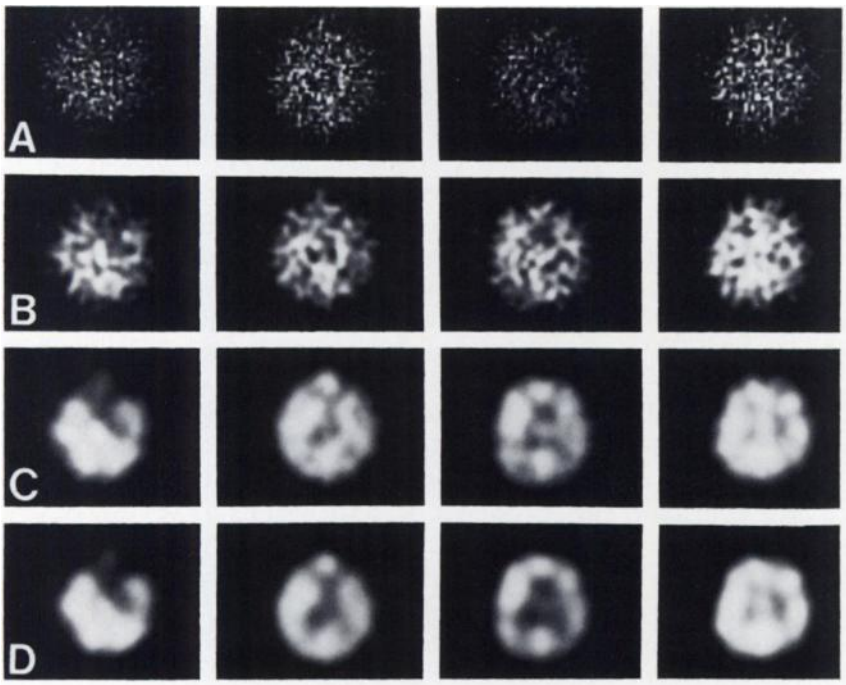

FIGURE 5
Selected reconstructed transverse slices from SPECT acquisition of ^{123}I-labeled iodamphetamine brain study. Row A: Ramp filter. Row B: Shepp-Logan filter with cutoff frequency of 0.66 times Nyquist frequency. Row C: Filtered by Metz filter optimized for ^{99m}Tc and LEHR collimator. Row D: Filtered by Metz filter optimized for ^{123}I and MEMS collimator. Defect in perfusion to frontal lobe seen in first slice on left can only be perceived with Metz filtering

myocardial perfusion (*7*) by standard gamma cameras should also be greatly enhanced by application of restoration filters.

The advantages of two-dimensional, prereconstruction filtering of SPECT studies have previously been discussed (*9*). One advantage was that the inclusion of count information from adjacent slices into the slice of interest helps increase the statistical certainty of data being processed. This accounts for a significant portion of the difference in the noise level between the images of Figs. 3–5. Simply adding slices together (increasing the slice thickness) would also accomplish a reduction in the noise level; however, it would also result in increasing the effective slice thickness (FWHM along body axis for transverse slices). As can be seen in Tables 2 and 3, two-dimensional prereconstruction filtering with restoration filters reduces the FWHM and FWTM within the slice and by implication also along the body axis since this is the Y-axis of the acquisition images. Thus, the two-dimensional deblurring of restoration filters is important because it allows one to decrease noise levels and the effective slice thickness at the same time.

In this study statistically significant decreases in the FWHM and FWTM of SPECT reconstructions of ^{111}In and ^{123}I line sources imaged by a MEMS collimator (Tables 2 and 3) were obtained with application of restoration filters when compared to the values obtained with only ramp filtering. This contrasts with previous results for less severely degraded images (*11*). When the FWHM and FWTM of a ^{99m}Tc line source imaged with a LEHR collimator were determined after prereconstruction filtering with an optimized Metz filter, no decrease in the FWHM and FWTM were observed even at the highest count level (*11*). However, the ^{99m}Tc values were much better to start with, as one would expect. The greater improvement in these measures of spatial resolution supports the initial hypothesis that digital restoration techniques can improve images made using medium- to high-energy photons more than images recorded using low-energy photons (^{99m}Tc).

When radionuclides which emit medium- to high-energy photons are imaged, the MTF will be degraded in two ways. First, septal penetration and scatter will cause a severe, rapid degradation of the system MTF at low frequencies. Second, the MTF will be attenuated due to the collimators used to diminish septal penetration and maintain sensitivity. These degradations of the performance of the imaging system in the low to mid spatial frequency range are well suited to correction by digital image restoration techniques. However, restoration filters cannot effectively correct for the higher frequency degradations because the noise dominates the signal at the higher frequencies. Thus, the degradation that occurs at these frequencies cannot be deconvolved without elevating noise levels and producing distracting noise textures.

It has been known for some time that scatter and septal penetration cause a sudden drop in the system MTF at low spatial frequencies (*17,25,26,28*). This alteration in the MTF by the inclusion of scatter and septal penetration can be modeled by noting that the primary, scatter, and septal penetration photons imaged can be considered as passing through three parallel transfer subsystems, each forming an image of the object (*32*). The total LSF is then the weighted sum of the LSF of each of these (*17,25*), as is the total optical transfer function (*32*). As long as the system is even (symmetric) and the optical transfer function of each component is non-negative, the total MTF will also be the weighted sum of the sub-system MTFs. To a first approximation the LSFs for each component can be represented as Gaussian functions, with that of the primary radiation being significantly sharper and taller than those of the scattered or septal penetration radiation. Since the Fourier transform of a Gaussian function is another Gaussian function with the width of the transform being inversely related to the width of the spatial domain form (*33*), the wide spatial domain scatter and septal penetration components become narrow frequency domain terms sitting on top of a wide frequency domain primary term (Figs. 1A and B). This explains how the wide spatial domain scatter and septal penetration LSFs become the respective narrow MTFs. In fact, the wider they are in the spatial domain, the narrower the resulting MTF will be.

The scaling of these components when adding them together is explained in the following manner. The "DC" or zero frequency component of each of these terms is just the integral of their respective LSFs (*33*). Thus the total system MTF can be expressed as (*25,26*):

$$MTF(f) = [MTF_G(f) + P \cdot MTF_P(f) + S \cdot MTF_S(f)]/[1 + P + S], \quad (5)$$

where MTF_G is the primary radiation component MTF (geometric), P is the penetration fraction (ratio of the "DC" term of the septal penetration to that of the primary radiation), MTF_P is the septal penetration component MTF, S is the scatter fraction (ratio of the "DC" term of scatter to that of the primary radiation), and MTF_S is the scattered radiation component MTF. From Eq. (5) it can be seen that the rapidly falling MTFs associated with septal penetration and scatter are added to that of the primary radiation, causing a significant decrease in the total MTF at low spatial frequencies. These are precisely the frequencies which can be deconvolved before restoration filters must decrease to avoid amplifying noise dominated terms (*15,19*). Hence, improvements in spatial resolution and image contrast are obtainable with restoration filters along with noise reduction (% FSD).

The reduction in the influence of scatter and septal penetration through the use of digital restoration filters

such as the Metz filter should facilitate attenuation correction and, hence, quantitation. One-dimensional frequency domain (*34*) or spatial domain (*35*) deconvolution of scatter has already been shown to aid attenuation correction and quantitation for ^{99m}Tc-labeled radiopharmaceuticals. The improved image quality obtained through use of optimized restoration filters should also facilitate edge-detection or image segmentation. This should result in an improved ability to do quantitation of volumes and activity; thus it is important to assess the impact on SPECT quantitation of the Metz or other restoration filters. Since these filters adapt to the image being filtered it is necessary to determine if such variability in the filter employed will have an adverse influence upon the reproducibility of quantitation. A study of two-dimensional, prereconstruction filtering of SPECT images in conjunction with quantitation is currently underway.

The MTFs used in forming the Metz filters of this paper were obtained from line sources 7.5-cm deep in Plexiglas scattering material. This is approximately the "effective" mean free path for ^{99m}Tc 140 keV photon; however, no such claim can be made for the ^{111}In and ^{123}I. We believe that further improvement in image quality for these radionuclides can be obtained by first determining the effective linear attenuation coefficient in a scattering medium for imaging these radionuclides (*36*), and then using the MTF determined from a line source placed at the depth corresponding to the "effective" mean free path.

CONCLUSION

A dramatic increase in image quality was observed with use of two-dimensional, prereconstruction Metz filtering of SPECT images of radionuclides which emit medium- to high-energy photons. The Metz filter was shown to be able to deconvolve septal penetration, scatter, and (to a lesser extent) point source blurring while suppressing noise, in a balanced manner.

FOOTNOTES

* Picker International (Dynascan 5C/61), Highland Heights, OH.

† Picker International, Ultrafine Collimator.

‡ Picker International, Gallium I Collimator.

§ Analogic Corp. (AP400), Peabody, MA.

¶ Picker International, SPETS-11 Reconstruction Software Package.

** Data Spectrum (Deluxe "SPECT Phantom"), Chapel Hill, NC.

ACKNOWLEDGMENTS

The authors thank Dr. L. Stephen Graham and Mr. Steven Cool for their advice and encouragement. They also thank Mrs. Linda Desai for her assistance in the preparation of this paper, and Medi-Physics, Inc. for providing the ^{123}I. This investigation was aided by a grant from the Whitaker Foundation.

REFERENCES

1. DeLand FH, Goldenberg DM: Diagnosis and treatment of neoplasms with radionuclide-labeled antibodies. *Semin Nucl Med* 15:2–11, 1985
2. Hnatowich DJ, Griffin TW, Kosciuczyk C, et al: Pharmacokinetics of an indium-111 labeled antibody in cancer patients. *J Nucl Med* 26:849–858, 1985
3. DeLand FH, Shih WJ: The status of SPECT in tumor diagnosis. *J Nucl Med* 25:1375–1379, 1984
4. Hill TC, Holman BL, Lovett R, et al: Initial experience with SPECT (single-photon computed tomography) of the brain using N-isopropyl I-123 p-iodoamphetamine. *J Nucl Med* 23:191–195, 1982
5. Kuhl DE, Barrio JR, Huang SC: Quantifying local cerebral blood flow by N-isopropyl-p-[I-123] iodoamphetamine (IMP) tomography. *J Nucl Med* 23:196–203, 1982
6. Shapiro B, Copp JE, Sisson JC, et al: Iodine-131 metaiodobenzylguanidine for the locating of suspected pheochromocytoma: Experience in 400 cases. *J Nucl Med* 26:576–585, 1985
7. Ryan JW, Harper PV, Resnekow L, et al: Single photon Rb-82 imaging of remote myocardial infarction. *J Nucl Med* 25:P52–P53, 1984 (abstr)
8. Kircos LT, Ortendahl DA, Hattner RS, et al: Comparison of planar images and SPECT with Bayesean preprocessing for the demonstration of facial anatomy and craniomandibular disorders. *J Nucl Med* 25:P71, 1984 (abstr)
9. King MA, Schwinger RB, Doherty PW, et al: Two-dimensional filtering of SPECT images using the Metz and Wiener filters. *J Nucl Med* 25:1234–1240, 1984
10. Webb S, Long AP, Ott RJ, et al: Constrained deconvolution of SPECT liver tomograms by direct digital image restoration. *Med Phys* 12:53–58, 1985
11. King MA, Schwinger RB, Penney BC: Variation in the count-dependent Metz filter with imaging system MTF. *Med Phys*13:139–149, 1986
12. Clarke LP, Qadir F, Al-Sheikh W, et al: Comparison of the physical characteristics of I-131 and I-123, with respect to differentiating the relative activity of the kidneys. *J Nucl Med* 24:683–688, 1983
13. Tyson RK, Amtey SR: Practical considerations in gamma camera line spread function measurement. *Med Phys* 5:480–484, 1978
14. Metz CE, Doi K: Transfer function analysis of radiographic imaging systems. *Phys Med Biol* 24:1079–1106, 1979
15. King MA, Doherty PW, Schwinger RB, et al: A Wiener filter for nuclear medicine images. *Med Phys* 10:876–880, 1983
16. Sanderson GK: Erroneous perturbations of the modulation transfer function derived from the line spread function. *Phys Med Biol* 13:661–663, 1968
17. Cradduck TD: Modulation transfer function and its application to radioisotope scanning. In *Advances In Medical Physics*, Laughlin JS, ed. Boston, The Second International Conference Medical Physics, 1971, pp 164–178
18. Hamming RW: *Digital Filters*, Englewood Cliffs, Prentice-Hall, 1977
19. King MA, Doherty PW, Schwinger RB, et al: Fast count-dependent digital filtering of nuclear medicine images. *J Nucl Med* 24:1039–1045, 1983

20. Metz CE: A mathematical investigation of radioisotope scan image processing. PhD Thesis, University of Pennsylvania, 1969
21. Metz CE, Beck RN: Quantitative effects of stationary linear image processing on noise and resolution of structure in radionuclide images. *J Nucl Med* 15:164–170, 1974
22. Larsson SA: Gamma camera emission tomography. *Acta Radiol* (Suppl) 363:7–15, 1980
23. Snedecor GW, Cochran WG: *Statistical Methods.* Sixth Edition, Ames, Iowa, The Iowa State University Press, 1967, pp 258–271
24. Brownlee KA: *Statistical Theory and Methodology,* Second Edition, New York, John Wiley and Sons, 1965, pp 309–318
25. Beck RN, Schuh MW, Cohen TD, et al: Effects of scattered radiation on scintillation detector response. In *Medical Radioisotope Scintigraphy,* Vol. 1, Vienna, IAEA, 1969, pp 595–616
26. Ehrhardt JC, Oberley LW, Lensink SC: Effect of a scattering medium on gamma-ray imaging. *J Nucl Med* 15:943–948, 1974
27. McKeighen RE, Muehllehner G, Mayer RA: Gamma camera collimator considerations for imaging 123-I. *J Nucl Med* 15:328–331, 1974
28. Bolmsjo MS, Persson BRR, Strand SE: Imaging 123-I with a scintillation camera. A study of detection performance and quality factor concepts. *Phys Med Biol* 22:266–277, 1977
29. Graham LS, Zielinski FW: Scintillation camera imaging with I-123. *Radiology* 130:519–523, 1979
30. Polak JF, English RJ, Holman BL: Performance of collimators used for tomographic imaging of I-123 contaminated with I-124. *J Nucl Med* 24:1065–1069, 1983
31. Madsen MT, Park CH: Enhancement of SPECT images by Fourier filtering the projection image set. *J Nucl Med* 26:395–402, 1985
32. Metz CE, Doi K: Transfer function analysis of radiographic imaging systems. *Phys Med Biol* 24:1079–1106, 1979
33. Bracewell RN: *The Fourier Transform and Its Applications.* New York, McGraw-Hill, 1978, pp 98–134
34. Floyd CE, Jazczak RJ, Greer KL, et al: Deconvolution of compton scatter in SPECT. *J Nucl Med* 26:403–408, 1985
35. Axelsson B, Masaki P, Israelsson A: Subtraction of Compton-scattered photons in single-photon emission computed tomography. *J Nucl Med* 25:490–494, 1984
36. Harris CC, Greer KL, Jazczak RJ: Tc-99m attenuation coefficients in water-filled phantoms determined with gamma cameras. *Med Phys* 11:681–685, 1984